Complex *Low*-Pass Filters

PETER KISS, VLADIMIR PRODANOV* AND JACK GLAS

Department of Communications Circuits Research, Agere Systems, 4 Connell Drive, Berkeley Heights, NJ 07922, USA
E-mail: kpeter@agere.com; vprodanov@agere.com; jpfglas@agere.com

Abstract. Zero-if transceivers suffer from the imbalance of the I and Q paths. By using a complex *low*-pass filter topology instead of a conventional pair of real low-pass filters, this imperfection can be reduced. Both analytical and numerical analysis show that the proposed technique is significantly more robust to circuit imperfections than the traditional architecture.

Key Words: complex filters, poliphase filters, sensitivity analysis, I/Q imbalance, direct conversion, zero if

1. Motivation

The performance of practical direct-conversion (zero-if) transceivers (Fig. 1(a)), among other imperfections, suffers from I/Q imbalance caused by the mismatch of the mixers and the imperfect quadrature signals from the local oscillators [1,2]. In addition, the mismatch between the frequency responses of the two real low-pass filters (LPF_1 and LPF_2 in Fig. 1(a)) also contributes to the I/Q imbalance of the receiver, causing performance degradation. When zero-if topology is proposed for wide-band applications with more stringent requirements (e.g., 802.11a where $SNR \cong 30$ dB) then this distortion needs to be taken into account.

In this paper a single complex low-pass filter (LPF_c in Fig. 1(b)) is proposed to reduce the I/Q imbalance due to the two-path filtering. Complex filters has been discussed for many years [3]. In the late 1960s, analog polyphase filters were proposed for single-sideband generators [4] and receivers [5]. About a decade later, their synthesis and analysis led to new developments [6–8]. Currently they are often used in low-if receiver ICs, e.g., [9–11].

Complex *low*-pass filters are a particular case of the popular complex *band*-pass filters [3–11]; however, as far as the authors are aware, the technical literature does not talk about them. Here, after a brief review of basic concepts, a detailed sensitivity analysis of such filters will be provided. This will demonstrate that complex low-pass filters outperform the pair of real low-pass filters from I/Q imbalance point of view—without adding significantly to the hardware complexity.

*Corresponding author.

2. Real Filters

In a conventional zero-if architecture [1,2], LPF_1 and LPF_2 form a two-input two-output linear network with complex input $x_c(t) \doteq x_1(t) + jx_2(t)$ and complex output $y_c(t) \doteq y_1(t) + jy_2(t)$ (Fig. 1(a), for details about complex signals refer to Appendix A). If the transfer functions of LPF_1 and LPF_2 are defined as $H_1(\omega) = \frac{B_1(\omega)}{A_1(\omega)}$ and $H_2(\omega) = \frac{B_2(\omega)}{A_2(\omega)}$, then

$$\begin{aligned} Y_c(\omega) &= \frac{A_2(\omega)B_1(\omega) + A_1(\omega)B_2(\omega)}{2A_1(\omega)A_2(\omega)}(X_1(\omega) \\ &\quad + jX_2(\omega)) + \frac{A_2(\omega)B_1(\omega) - A_1(\omega)B_2(\omega)}{2A_1(\omega)A_2(\omega)} \\ &\quad \times (X_1(\omega) - jX_2(\omega)) \\ &= H_{cm}(\omega)X_c(\omega) + H_{df}(\omega)X_c^*(-\omega) \end{aligned} \tag{1}$$

Equation (1) shows that the input complex signal $x_c(t)$ is processed in a parallel fashion by $h_{cm}(t)$ and $h_{df}(t)$ (Fig. 2(a)). The common component of $H_1(\omega)$ and $H_2(\omega)$ forms $H_{cm}(\omega)$ which gives the desired (direct) output $H_{cm}(\omega) \cdot X_c(\omega)$. However, if $H_1(\omega)$ and $H_2(\omega)$ are not identical, then a nonzero $H_{df}(\omega)$ contributes to a leakage (undesired or difference) output component $H_{df}(\omega) \cdot X_c^*(-\omega)$.

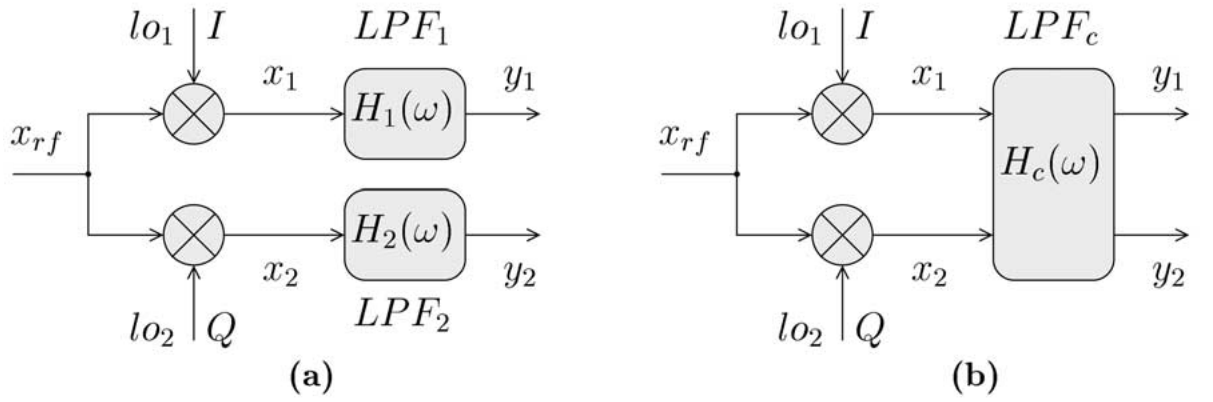

Fig. 1. Quadrature direct conversion receiver with (a) two real low-pass filters; (b) one complex low-pass filter.

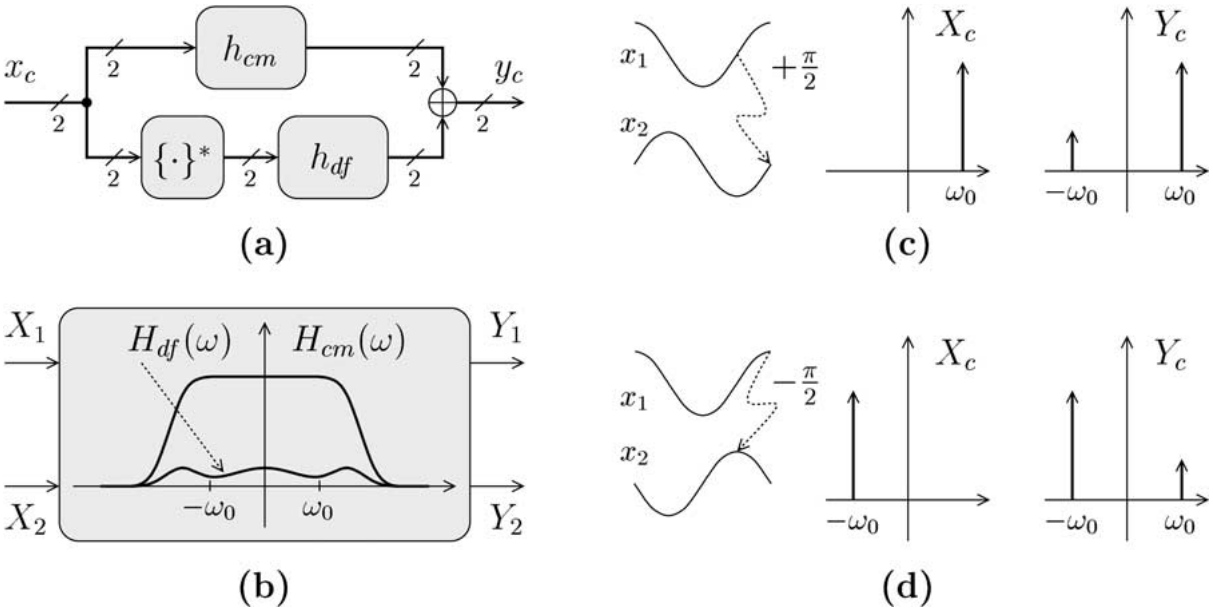

Fig. 2. (a) Time-domain and (b) frequency-domain model of an imperfect two-path low-pass filter. Imperfect filtering of a complex (c) positive-frequency and (d) negative-frequency input tone.

For example, if a complex positive-frequency tone at ω_0 undergoes an imperfect two-path filtering operation, then the complex output will contain, besides the desired component at ω_0, a leakage component at $-\omega_0$ (Fig. 2(c)). Similarly, a complex input tone at $-\omega_0$ will leak into ω_0 (Fig. 2(d)).

Let $X_p(\omega)$ and $X_n(\omega)$ denote the positive and negative frequency content of $X_c(\omega)$, respectively (Fig. 3(b)). Usually, $X_p(\omega)$ and $X_n(\omega)$ correspond to the desired signal and the undesired image, respectively. The imperfect two-path filtering, expressed by equation (1), means that a fraction of the positive-frequency signal $X_p(\omega)$ will be transformed into a negative-frequency signal $X_p^*(-\omega)$ which leaks on top of $X_n(\omega)$ and distorts it (Fig. 3). Similarly, a fraction of $X_n^*(-\omega)$ distorts $X_p(\omega)$.

Note that this distortion occurs even if the complex local oscillator signal LO_c is a single complex tone

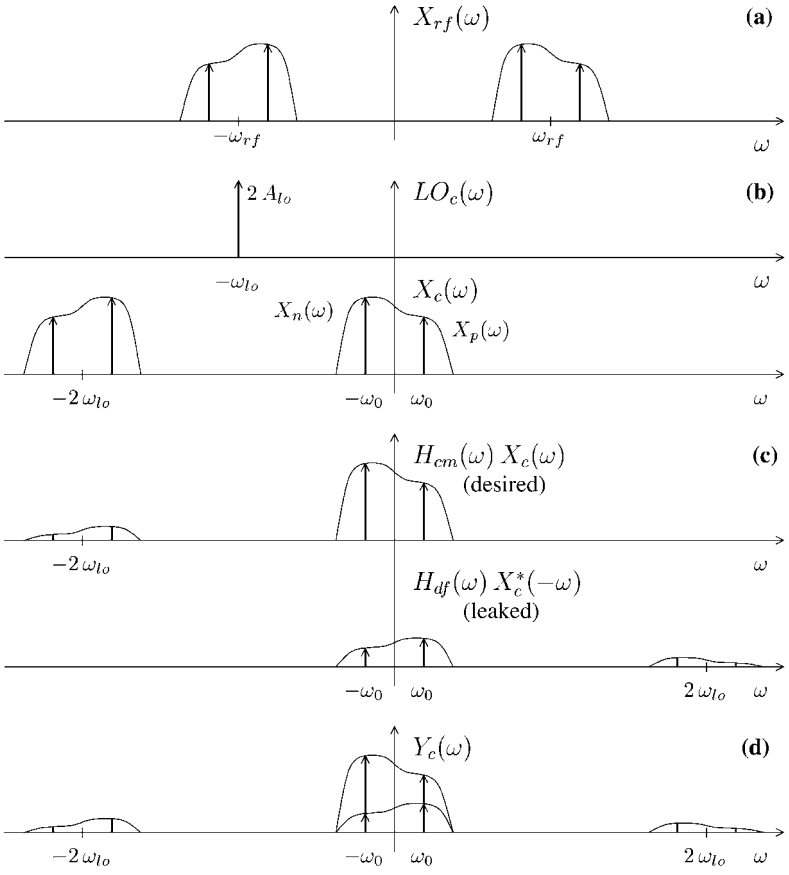

Fig. 3. Signal processing: (a) rf input signal; (b) ideal zero-if I/Q mixing; (c) filtering: desired and leakage signals; (d) output signal distorted by imperfect I/Q filtering.

at $-\omega_{lo}$, as it was assumed in Fig. 3(b). In practical situations, when LO_c is not a perfect quadrature, then the effects of both imperfections add.

3. Complex Filters

A complex filter is a two-input two-output linear network which frequency response is not necessarily symmetrical with respect to dc ($\omega = 0$). Its gain and phase responses are functions both of the frequency and the relative phase difference of the two real inputs x_1 and x_2 (Fig. 1(b)).

As an example, a fourth-order all-pole band-pass complex filter with bandwidth BW centered around ω_{if} is shown in Fig. 4(a). Since $H_c(\omega)|_{\omega\in BW} \cong 0$ dB and $H_c(-\omega)|_{\omega\in BW} \ll 0$ dB, the complex band-pass filter provides image rejection in addition to filtering—without adding significantly to the hardware complexity of the filter.

A complex low-pass filter is a particular case of the popular complex band-pass filter when $\omega_{if} = 0$ (Fig. 4(b)). Note that every complex pole is doubled and one of them is cancelled by a complex zero. The ideal response of such a filter can be designed to be identical to the ideal response of the pair of LPF_1 and LPF_2.

3.1. "Single" Complex Pole

The circuit implementation of complex filters involves realizing non-complex-conjugate (single) complex poles. This can be achieved by a pair of complex conjugate poles out of which one is cancelled by a single complex zero [6] (Fig. 4).

A "single" complex pole can effectively be implemented using two integrators in a feedback loop with

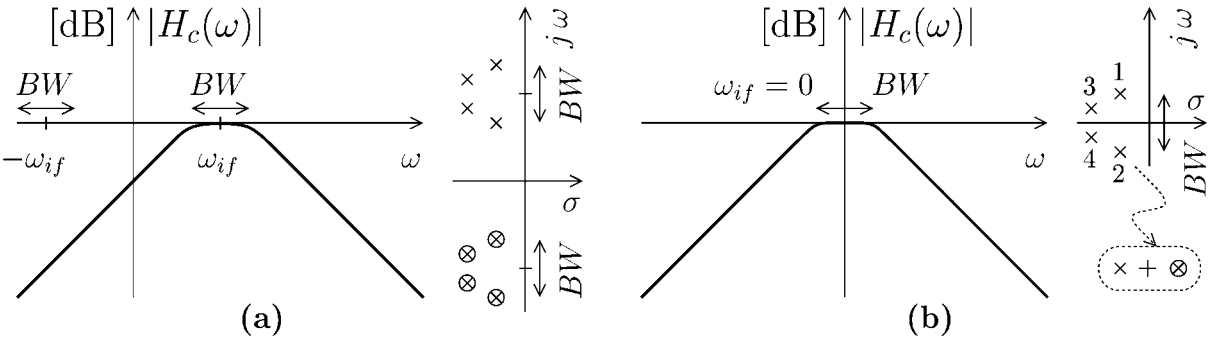

Fig. 4. Frequency response and pole-zero constellation for a 4th-order (a) complex band-pass filter; (b) complex low-pass filter.

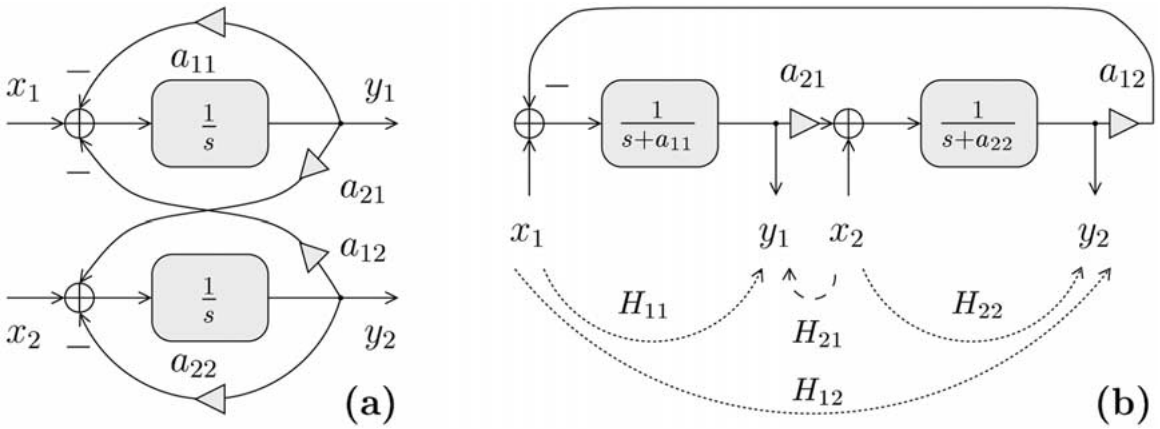

Fig. 5. First-order complex filter implementing a "single" complex pole.

two inputs and two outputs [8] (Fig. 5(a)). The complex output becomes

$$Y_c(s) \doteq \frac{s+a_{22}+ja_{21}}{D(s)}X_1(s) + \frac{s+a_{11}+ja_{12}}{D(s)}jX_2(s) \tag{2}$$

where $D(s) = s^2 + (a_{11}+a_{22})s + a_{11}a_{22} + a_{12}a_{21}$ (for details of obtaining equation (2) refer to Appendix B). In ideal case, i.e., $a_{11} = a_{22} = a$ and $a_{12} = a_{21} = b$, equation (2) becomes

$$\begin{aligned} Y_{cid}(s) &= \frac{s+a+jb}{(s+a+jb)(s+a-jb)}(X_1(s)+jX_2(s)) \\ &= \frac{1}{s+a-jb}X_c(s) = H_{id1}(s)X_c(s) \end{aligned} \tag{3}$$

Equation (3) shows that the first-order ideal complex filter $H_{id1}(s)$ implements a "single" complex pole $p = -a+jb$, based on a perfect pole cancellation by the zero $z = -a-jb$.

Due to circuit imperfections, usually $a_{11} \neq a_{22} \neq a$ and $a_{12} \neq a_{21} \neq b$, so the pole-zero cancellation does not hold. Equation (2) can be written as follows (similar to [12, p. 58])

$$\begin{aligned} Y_c(s) &= \frac{s + \frac{a_{11}+a_{22}}{2} + j\frac{a_{12}+a_{21}}{2}}{D(s)}(X_1(s)+jX_2(s)) \\ &\quad + \frac{\frac{a_{11}-a_{22}}{2} + j\frac{a_{12}-a_{21}}{2}}{D(s)}(X_1(s)-jX_2(s)) \\ &= H_{cm}(s)X_c(s) + H_{df}(s)X_c^*(s^*) \end{aligned} \tag{4}$$

$$\Rightarrow \quad Y_c(\omega) = H_{cm}(\omega)X_c(\omega) + H_{df}(\omega)X_c^*(-\omega) \tag{5}$$

Since this last result is identical with equation (1), a complex filter behaves in the same way as a pair of real filters, so it can be modeled by Fig. 2(a). Also, a mismatched complex filter causes distortion as explained earlier and illustrated by Fig. 3. However, note that $H_{cm}(\omega)$ and $H_{df}(\omega)$ have real coefficients in equation (1), but they have complex ones in equation (5). Therefore, $H_{cm}(\omega)$ and $H_{df}(\omega)$ are even functions in

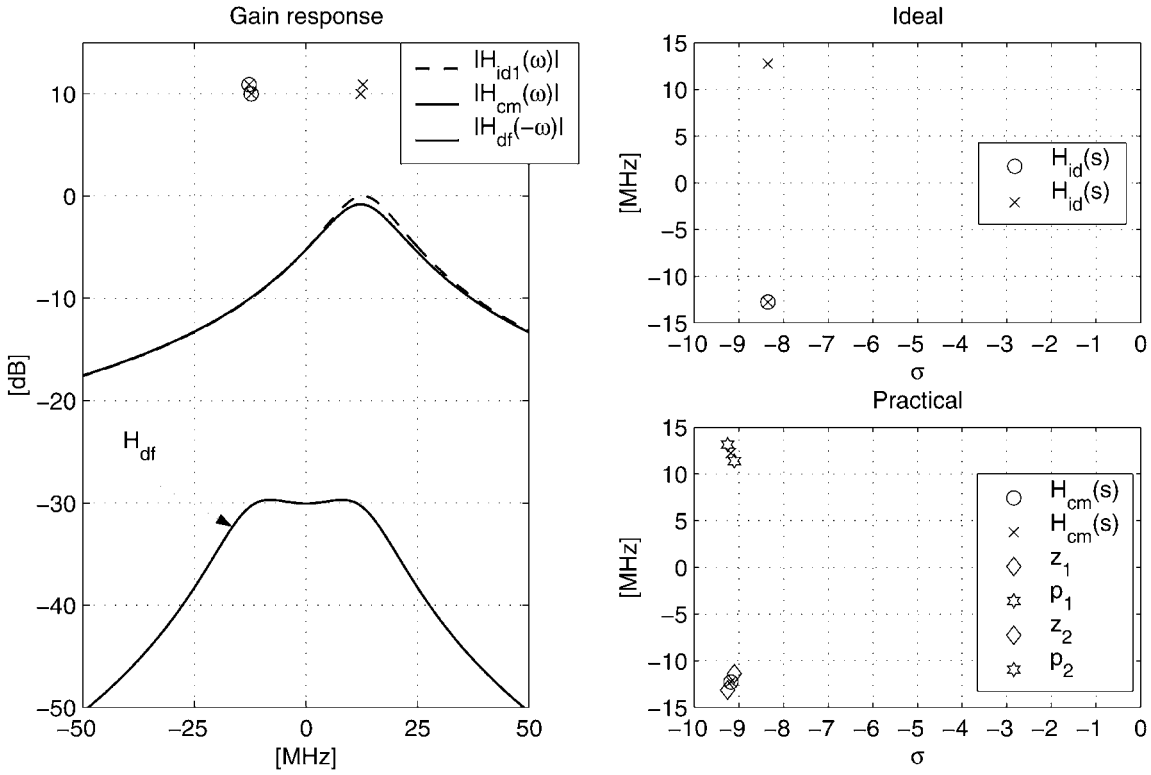

Fig. 6. First-order complex band-pass filter with $f_{if} = 13$ MHz and $\sigma_n = 5\%$ mismatch; $z_1 = -a_{11} - ja_{12}$, $p_1 = -a_{11} + ja_{12}$, $z_2 = -a_{22} - ja_{21}$, and $p_2 = -a_{22} + ja_{21}$.

ω in equation (1), but they are asymmetrical in ω in equation (5).

The coefficients a_{11}, a_{12}, a_{21} and a_{22} in Fig. 5(a) are realized by various circuit elements depending on their implementations (e.g., passive *R-C* [5], active *R-C* [8], g_m-*C* [11], etc.). Here, a normally-distributed error with 1% variance was considered for each coefficient; the errors were assumed to be uncorrelated. Therefore, the magnitude and distribution of the errors need to be tailored to the specifics of the implementation.

The **simulated** behavior of an imperfect *versus* perfect "single" complex pole is shown in Fig. 6 (similar plots can be found in [12, p. 59]). The ideal pole-zero constellation presents a perfect pole-zero cancellation, and the frequency response $H_{id1}(\omega)$ looks as expected. In the presence of 5% errors[1] the poles p_1 and p_2 of the filter move away from the ideal value of p which leads to a nonzero $H_{df}(s)$. However, the pole-zero cancellation within $H_{cm}(s)$ occurs at a high degree (for details refer to Appendix C).

Note that the simulations were performed using a *black-box* approach. In this method a perfect quadrature complex signal, i.e., $x_c(t) = A\cos(\omega_0 t) + jA\sin(\omega_0 t)$, was applied to the input of the filter. The spectrum of the resulting complex output $y_c(t)$ was measured at ω_0 and $-\omega_0$, providing the values for $H_{cm}(\omega_0)$ and $H_{df}(-\omega_0)$, respectively. The experiment was performed for all the range of frequencies of interest. In addition, the transfer functions $H_{cm}(\omega)$ and $H_{df}(\omega)$ were calculated based on equation (4). The numerical and analytical results were identical which proved the validity of the model described by equation (4). Equations (6) and (7), defined and discussed later, were verified and validated by a similar simulation procedure.

4. Cascade of Filters

High-order transfer functions can be realized by a cascade arrangement of elementary building blocks. For example, a fourth-order all-pole complex low-pass filter (CLPF) can be built from four "single" complex poles, while a similar pair of real low-pass filters (RLPF) uses four biquads (Fig. 7). Both

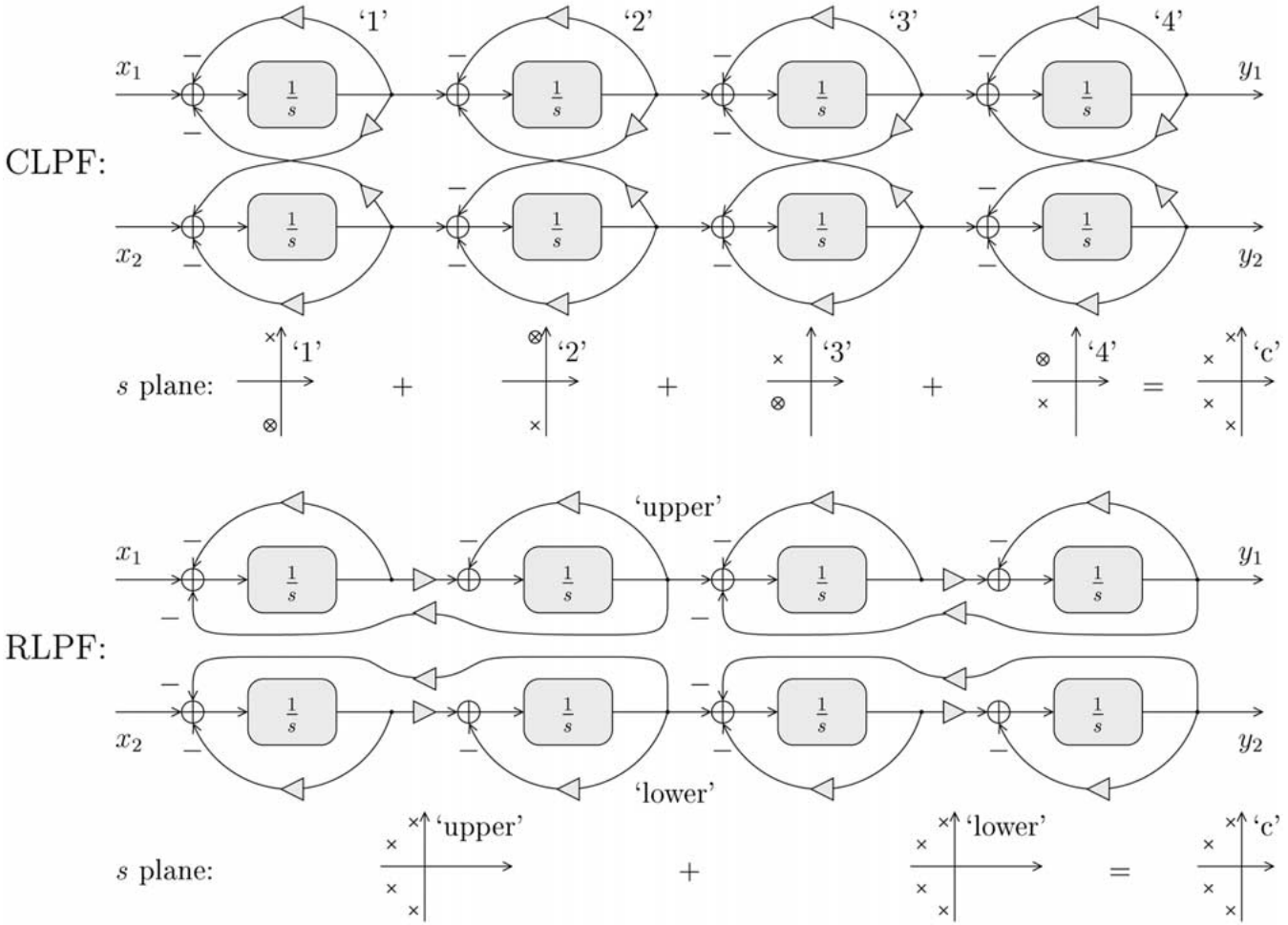

Fig. 7. Two possible implementation of a fourth-order complex low-pass filter.

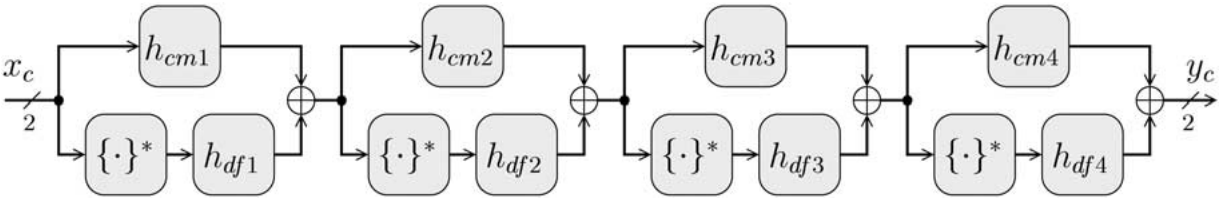

Fig. 8. Parallel model for a cascade of imperfect complex poles.

implementations need eight integrators, thus the hardware complexity is roughly the same. Note that for a pair of RLPFs there is no interaction between the individual I and Q stages but at the global output (Fig. 7). Therefore, its leakage, i.e., $H_{df}(\omega)$, depends only on the global transfer function of LPF_1 and LPF_2, and equation (1) holds for any order of the filters.

On the other hand, for a cascade of CLPFs the desired (direct) and undesired (leakage) signal components interact at the output of every stage (Fig. 8). Therefore, each of the four stages processes its complex input and provides desired and undesired output, according to equation (5) and illustrated by simulation results in Fig. 6. Due to this leakage mechanism, the image signal component of the input leaks into the desired signal, and vice versa. Moreover, the signal may leak more than *once* contributing accordingly to the global transfer functions.

Therefore,

$$H_{cm}(s) = H_{cm4}(s)H_{cm3}(s)H_{cm2}(s)H_{cm1}(s) + H_{df4}(s)H^*_{df3}(s^*)H_{cm2}(s)H_{cm1}(s) + \cdots \tag{6}$$

$$H_{df}(s) = H_{df4}(s)H^*_{cm3}(s^*)H^*_{cm2}(s^*)H^*_{cm1}(s^*) + H_{cm4}(s)H_{df3}(s)H^*_{cm2}(s^*)H^*_{cm1}(s^*) + H_{cm4}(s)H_{cm3}(s)H_{df2}(s)H^*_{cm1}(s^*) + H_{cm4}(s)H_{cm3}(s)H_{cm2}(s)H_{df1}(s) + \cdots \tag{7}$$

$H_{cm}(\omega)$ and $H_{df}(\omega)$ contain even and odd numbers of time-domain[2] complex conjugate operations on the input signal $x_c(t)$, respectively. According to equation (7), the leakage of CLPFs is given by a combination of the individual transfer functions. Therefore, there is a degree of freedom to sequence the individual stages in order to minimize the global $H_{df}(\omega)$.

4.1. Comparative Sensitivity Analysis

Replacing a pair of RLPFs LPF_1 and LPF_2 with a CLPF in a direct-conversion receiver (Figs. 1(a) vs. (b)) is motivated by the expected increased robustness of the latter. A comparative sensitivity analysis will be presented in the following.

As an example, two imperfect RLPF and CLPF are compared in Fig. 9. Both are fourth-order 8.5-MHz Chebyshev all-pole filters with a pass-band ripple of $R_p = 1$ dB. They are affected by a normally distributed error with $\sigma_n = 5\%$, so their poles lay in clusters around the ideal locations. For the filters (i.e., LPF_1, LPF_2 and CLPF) cascade (as opposed to, e.g., ladder) implementations were assumed. Note that $H_{cm}(\omega)$ and $H_{df}(\omega)$ are even functions in ω for RLPFs, but they are asymmetrical in ω for CLPFs.

One can define the average image-rejection ratio over a bandwidth BW as

$$IMR = 10\log_{10}\int_{\omega\in BW}\left|\frac{H_{cm}(\omega)}{H_{df}(\omega)}\right|^2 d\omega \quad \text{(dB)} \tag{8}$$

which shows how effectively a complex filter passes signal inputs while rejecting image inputs [12, p. 59]. The RLPF and CLPF lead to $IMR_r = 15.8$ dB and $IMR_c = 23.0$ dB, respectively. Therefore, the complex filter is 7.2 dB better than the pair of real filters in this example. However, these are just partial results. In order to draw general conclusions, the experiment presented in Fig. 9 was repeated for several mismatch states (as in a Monte-Carlo type analysis) and the results were processed statistically. Moreover, the effect of the sequence of stages was investigated—presented next.

4.2. Sequence of Complex Poles in CLPFs

The sequence of the stages plays a significant role in the complex filter's performance. From equation (4)

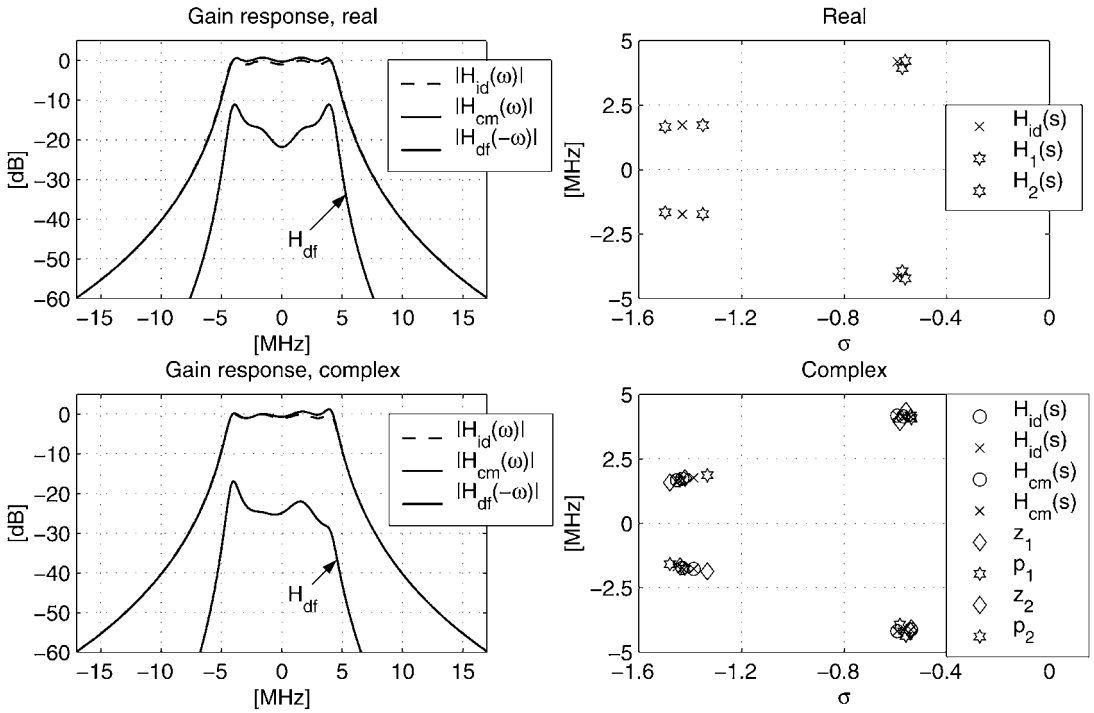

Fig. 9. RLPF versus CLPF for $N = 4$th order.

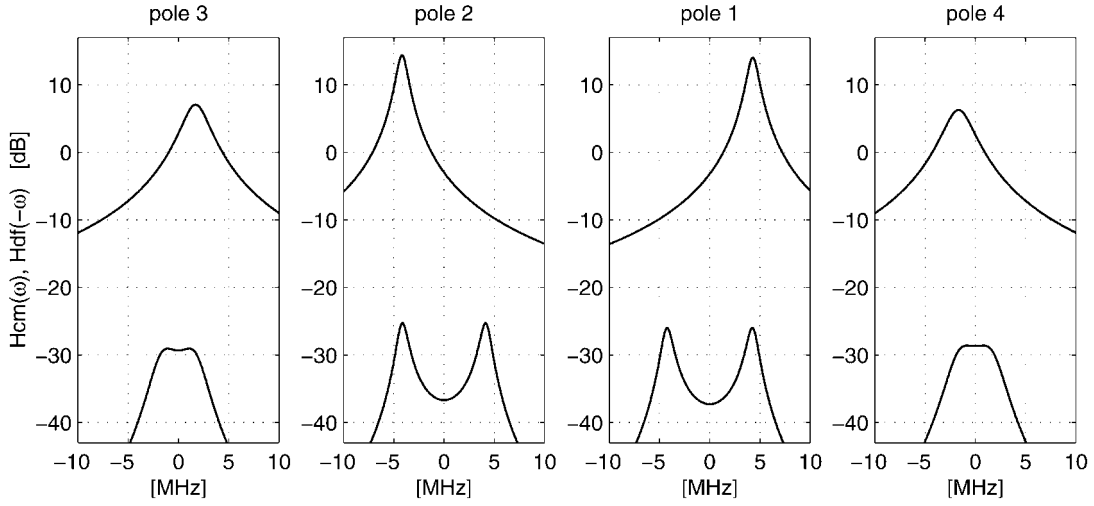

Fig. 10. Simulation example for a cascade of four complex stages.

results that the magnitude of one stage's leakage is proportional to the quality factor Q, i.e., $Q = \frac{1}{2a}\sqrt{a^2+b^2}$, of the pole it implements. Should the stages, therefore, be ordered in a reverse sequence of their pole Q-s?

In order to minimize the total leakage at the output of a cascaded CLPF, the "leakage gain" seen by the most sensitive pole(s) needs to be minimized. This is illustrated for a fourth-order filter in Fig. 10. The leakage of the pole 2 is given by $H_{df2}(\omega)$ which sees a leakage gain of $H^*_{cm3}(-\omega)H_{cm1}(\omega)H_{cm4}(\omega)$. This gain is evenly distributed for positive and negative frequencies, so it has the lowest possible average value. The

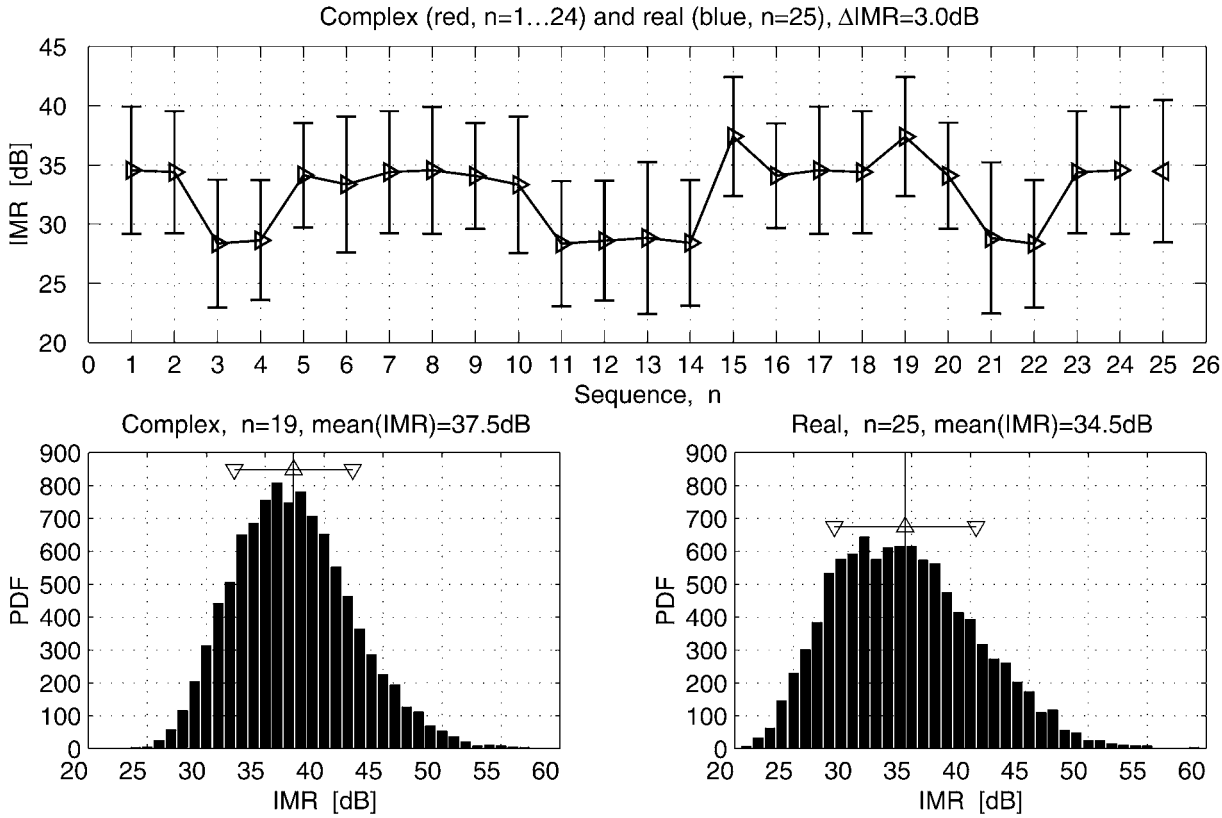

Fig. 11. The effect of ordering the poles in CLPF for $N = 4$.

same is true for the other high-Q pole 1. Next, this intuitive reason will be verified by numerical methods.

Figure 11 presents the results of a statistical analysis. The variable n indicates the sequence of stages (each stage implements an imperfect complex pole); the behavior of all $4! = 24$ possible permutations are shown. The poles are labeled $1 \ldots N$, sequenced in a decreasing order of their Q-s, but first the pole on the positive side of ω comes, then that one on the negative side of ω follows (Fig. 4(b)). The pole sequences corresponding to different n-s are given in Table 1. For example, $code(15) =$ 3-2-1-4 means that pole 3 is implemented in the first stage followed by pole 2, pole 1, and pole 4, like in Fig. 10. In Fig. 8 the poles were arranged according to $n = 1$, i.e., $code(1) =$ 1-2-3-4. $n = 25$ is for RLPF. For each sequence n, a set of 10000 normally distributed ($\sigma_n = 1\%$) random mismatch states were simulated which error-bar (mean value and variance) is shown in Fig. 11. On the lower part of this figure, two histograms of *IMR* are shown for $n = 19$ (CLPF) and $n = 25$ (RLPF), respectively. Note that CLPF has a larger mean and lower variance than RLPF.

Table 1. All 24 permutations of four poles.

n	$code(n)$	n	$code(n)$	n	$code(n)$	n	$code(n)$
1	1-2-3-4	7	2-1-3-4	13	3-1-2-4	**19**	**4-1-2-3**
2	1-2-4-3	8	2-1-4-3	14	3-1-4-2	20	4-1-3-2
3	1-3-2-4	9	2-3-1-4	**15**	**3-2-1-4**	21	4-2-1-3
4	1-3-4-2	10	2-3-4-1	16	3-2-4-1	22	4-2-3-1
5	1-4-2-3	11	2-4-1-3	17	3-4-1-2	23	4-3-1-2
6	1-4-3-2	12	2-4-3-1	18	3-4-2-1	24	4-3-2-1

Based on the *IMR* performance of CLPFs shown in Fig. 11, three categories of CLPFs can be clearly identified: "best" ($n \in \{15, 19\}$), "mediocre" ($n \in \{1, 2, 5–10, 16–18, 20, 23, 24\}$), and "worst" ($n \in \{3, 4, 11–14, 21, 22\}$). In the "best" group the poles follow a *shoestring* pattern. There are only two such sequences possible, i.e., $code(15) =$ 3-2-1-4 and $code(19) =$

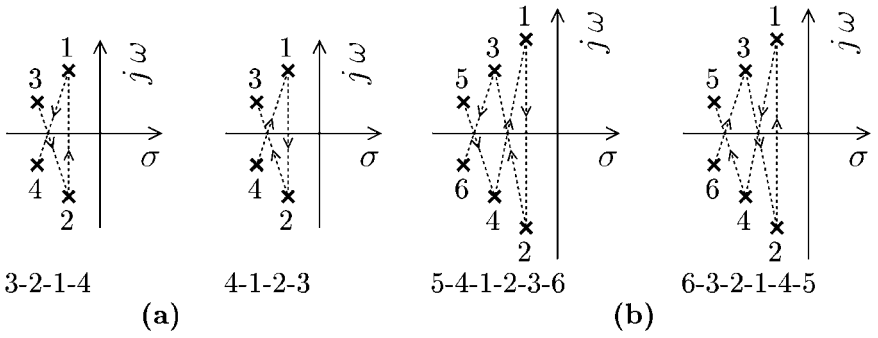

Fig. 12. Shoestring patterns of poles for (a) $N = 4$; (b) $N = 6$.

4-1-2-3 (Fig. 12(a)). Indeed, these sequences minimize the "leakage gain" seen by the most sensitive poles. Finally, Fig. 11 shows that the best sequenced CLPFs achieve about 3 dB larger *IMR* compared to RLPFs for $N = 4$. Note that this result depends on the highest value of the pole Q-s; for the filter in Fig. 9, $Q_{\max} = 3.5$. If a ripple of 3 dB is assumed, which boosts up the $Q_{\max}$ to 5.5, then ΔIMR becomes 4.1 dB. Therefore, the proposed technique is more effective for high-Q (i.e., more selective) filters.

The histograms of Fig. 11 allow determining the yield of such filters (Fig. 13). These curves reveal a more dramatic comparison. For example, if an application requires an *IMR* of 30 dB, then using RLPFs vs. CLPFs will result of about 20% lower yield. Moreover, if a mass production needs to achieve a yield not lower than 90%, using CLPFs vs. RLPFs provides an excess of 4 dB of *IMR*.

The benefits of using CLPF over RLPF improve when the filter's order increases; note that high-order

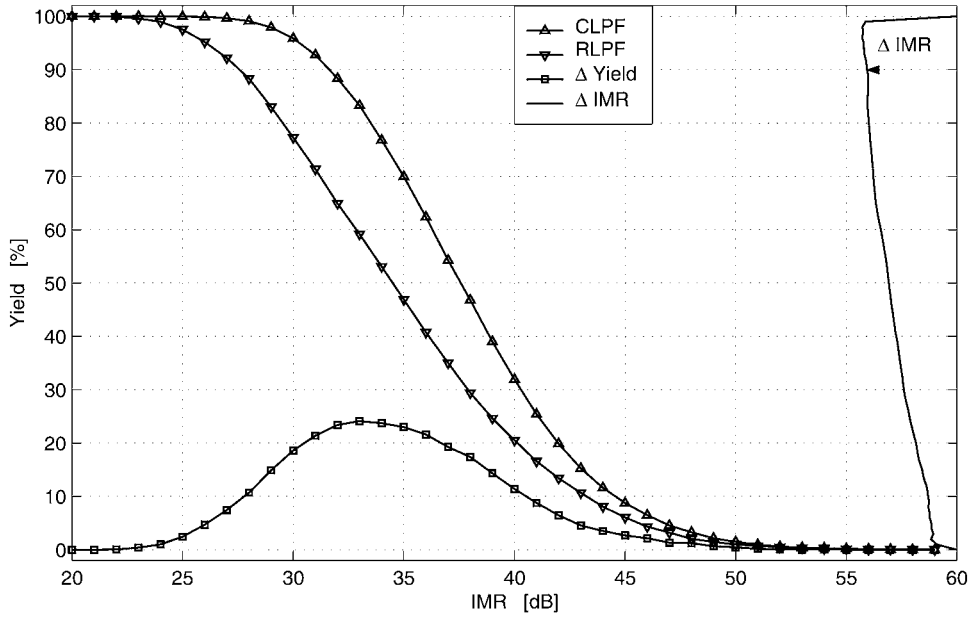

Fig. 13. Comparative yield curves for $N = 4$ (data from Fig. 12).

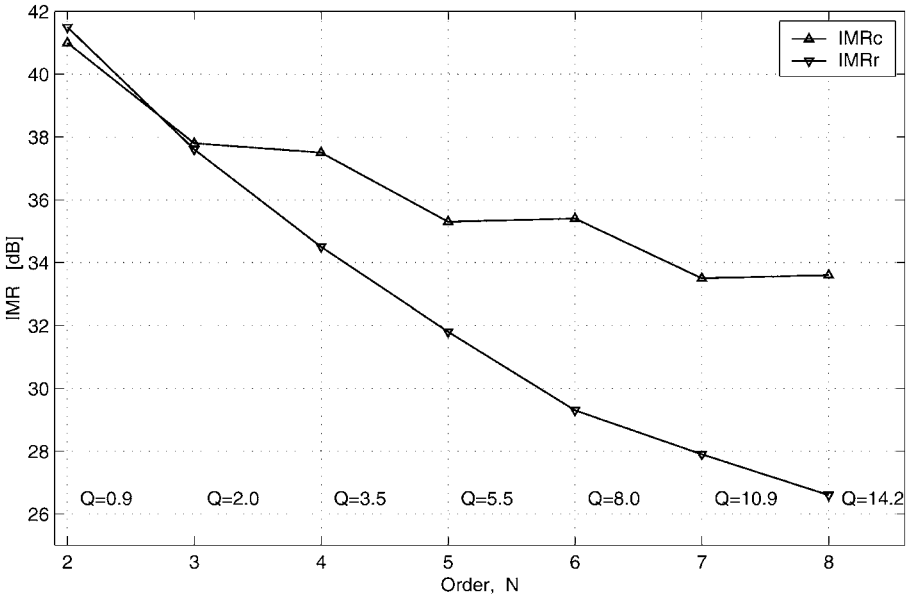

Fig. 14. CLPF versus RLPF in function of N.

Table 2. CLPF *versus* RLPF in function of N.

N, order	2	3	4	5	6	7	8
$Q_{\max}$	0.9	2.0	3.5	5.5	8.0	10.9	14.2
$\overline{IMR_c}$ (dB)	41.0	37.8	37.5	35.3	35.4	33.5	33.6
$\overline{IMR_r}$ (dB)	41.5	37.6	34.5	31.8	29.3	27.9	26.6
$\Delta\overline{IMR}$ (dB)	**−0.5**	**0.2**	**3.0**	**3.5**	**6.1**	**5.6**	**7.0**

filters are more likely to use high-Q poles. This is summarized in Table 2 and Fig. 14, e.g., the improvement is about 7 dB for $N = 8$. It is interesting to note that the number of poles, thus the selectivity, of an odd-order CLPF can be incremented for "free," while this costs *IMR* degradation in the case of RLPFs (Fig. 14).

It was verified by simulations that in the case of high-order filters, the above-described shoestring criteria for choosing the best sequence for CLPF remains valid. For example, for $N = 6$ the two best sequences should be 5-4-1-2-3-6 and 6-3-2-1-4-5 (Fig. 12(b)). For odd-order filters, the position of the real pole does not matter much since its leakage is small and its response is symmetrical in respect to dc. However, it is preferred to place the real pole in the middle or at the extremes (i.e., beginning or end) of the cascade in order to keep the shoestring pattern symmetrical. For $N = 2$ and $N = 3$ the CLPF is unbalanced, and it performs similar to the RLPF (Table 2).

In summary, the intuitive and statistical analysis presented in this section demonstrated that it is possible to predict *a priori* the most robust CLPF topology. Also, it turns out that the CLPFs are significantly less sensitive to circuit imperfections than RLPFs.

5. Conclusions

The proposed complex low-pass filter is a novel topology suitable for direct-conversion transceivers. Detailed analytical and numerical analysis were presented. In order to reach maximal robustness for a complex low-pass filter, its stages should be ordered in an a priori predictable shoestring pattern. It turns out that the complex low-pass filters are several dB-s more robust to circuit imperfections than the traditionally used pair of real low-pass filters. Moreover, the proposed technique is even more effective for high-order high-Q filters.

Appendix

A. Complex Exponential

The complex exponential $Ae^{j\omega_0 t}$ can be considered as the mathematical model of a perfect quadrature

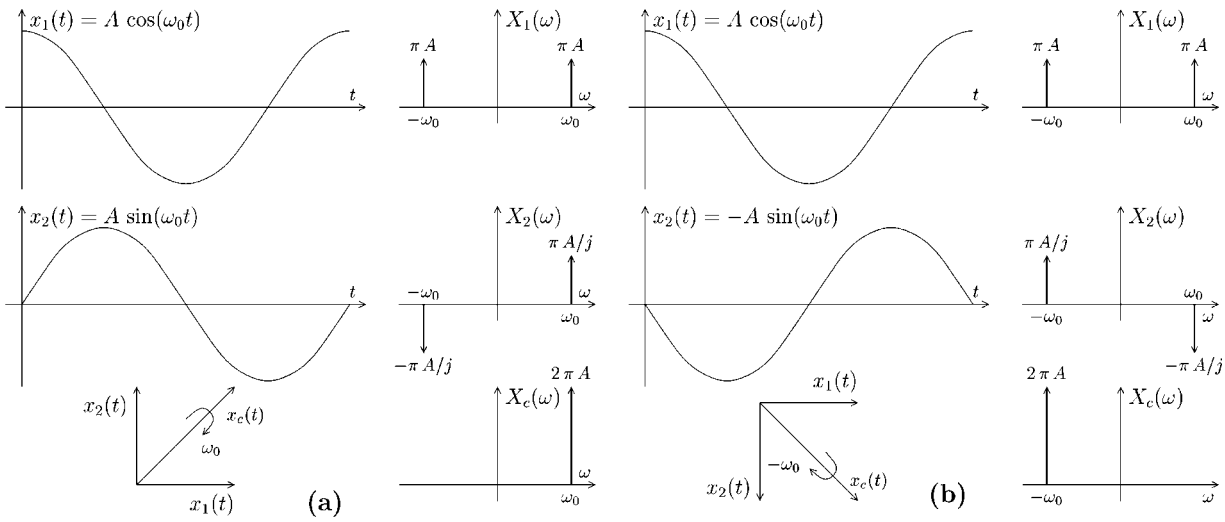

Fig. 15. Complex exponentials formed by a pair of (a) forward-quadrature signals, $X_c(\omega) = \mathcal{F}\{A\cos(\omega_0 t) + jA\sin(\omega_0 t)\}$; (b) reverse-quadrature signals, $X_c(\omega) = \mathcal{F}\{A\cos(\omega_0 t) - jA\sin(\omega_0 t)\}$.

oscillation. It is generated by two real signals x_1 and x_2 (Fig. 15(a)) which oscillate with the same angular frequency ω_0 and amplitude A. They should be in a quadrature relationship,[3] that is, $x_2(\phi_2(t)) = x_1(\phi_1(t) - \frac{\pi}{2})$, for $\forall t > 0$; x_2 is the Hilbert transform [14, Section 11.4] of x_1, and $(x_1,\ x_2)$ can be called a forward-quadrature pair, $\uparrow_{\rightarrow}$. From the two real signals x_1 and x_2, the complex signal x_c is obtained by the $x_c(t) \doteq x_1(t) + jx_2(t)$ operation. In other words, $\mathrm{Re}\{x_c(t)\} = x_1(t)$ and $\mathrm{Im}\{x_c(t)\} = x_2(t)$. x_c is also called the analytic part [15, p. 119] of x_1. It is convenient to represent x_c as a forward-quadrature or forward-rotating phasor, which rotates clockwise with ω_0, and x_1 always leads x_2 with $\frac{\pi}{2}$ radians satisfying the quadrature relationship. The time-frequency representation of these signals is given graphically in Fig. 15(a), and analytically below

$$\begin{cases} x_1(t) = A\cos(\omega_0 t) & \leftrightarrow X_1(\omega) = A\pi\{\delta(\omega + \omega_0) + \delta(\omega - \omega_0)\} \\ x_2(t) = A\sin(\omega_0 t) & \leftrightarrow X_2(\omega) = -(A\pi/j) \times \{\delta(\omega + \omega_0) - \delta(\omega - \omega_0)\} \\ x_c(t) \doteq x_1(t) + jx_2(t) & \leftrightarrow X_c(\omega) = 2A\pi\delta(\omega - \omega_0) \end{cases} \tag{9}$$

Note that x_c is a *double*-wired signal and its Fourier transform $X_c(\omega)$ is a *single* Dirac delta function at ω_0 (Fig. 15(a)).

When x_1 lags x_2 with $\frac{\pi}{2}$ radians (or x_2 leads x_1 with $\frac{\pi}{2}$), $(x_1,\ x_2)$ can be called a reverse-quadrature pair, $\downarrow^{\rightarrow}$. x_c can be represented by a reverse-quadrature or reverse-rotating phasor, which rotates clockwise with $-\omega_0$ (or counter-clockwise with ω_0), and forms the complex exponential $Ae^{-j\omega_0 t}$ (Fig. 15(b))

$$\begin{cases} x_1(t) = A\cos(\omega_0 t) & \leftrightarrow X_1(\omega) = A\pi\{\delta(\omega + \omega_0) + \delta(\omega - \omega_0)\} \\ x_2(t) = -A\sin(\omega_0 t) & \leftrightarrow X_2(\omega) = (A\pi/j) \times \{\delta(\omega + \omega_0) - \delta(\omega - \omega_0)\} \\ x_c(t) \doteq x_1(t) + jx_2(t) & \leftrightarrow X_c(\omega) = 2A\pi\delta(\omega + \omega_0) \end{cases} \tag{10}$$

Note that the Fourier transform $X_c(\omega)$ is a single Dirac delta function at $-\omega_0$ (Fig. 15(b)).

B. "Single" Complex Pole

An effective implementation of a "single" complex pole can be done using two integrators within a feedback loop with two inputs and two outputs (Fig. 5(a)). This diagram is redrawn in Fig. 5(b) which emphasizes on the negative feedback loop used. The amount of feedback [16, Section 8.1] is given by

$$\begin{aligned} \text{“}1 + \beta A\text{”} &= 1 + \frac{a_{12}a_{21}}{(s + a_{11})(s + a_{22})} \\ &= \frac{s^2 + (a_{11} + a_{22})s + a_{11}a_{22} + a_{12}a_{21}}{(s + a_{11})(s + a_{22})} \\ &= \frac{D(s)}{(s + a_{11})(s + a_{22})} \end{aligned} \tag{11}$$

The voltage-gain parameters[4] H of this circuit are the following

$$\begin{cases} H_{11} \doteq \left.\dfrac{Y_1(s)}{X_1(s)}\right|_{x_2=0} = \dfrac{1}{s+a_{11}} \cdot \dfrac{1}{1+\beta A} = \dfrac{s+a_{22}}{D(s)} \\ H_{12} \doteq \left.\dfrac{Y_2(s)}{X_1(s)}\right|_{x_2=0} = \dfrac{a_{21}}{(s+a_{11})(s+a_{22})} \cdot \dfrac{1}{1+\beta A} \\ \qquad\qquad = \dfrac{a_{21}}{D(s)} \\ H_{21} \doteq \left.\dfrac{Y_1(s)}{X_2(s)}\right|_{x_1=0} = \dfrac{-a_{12}}{(s+a_{11})(s+a_{22})} \cdot \dfrac{1}{1+\beta A} \\ \qquad\qquad = \dfrac{-a_{12}}{D(s)} \\ H_{22} \doteq \left.\dfrac{Y_2(s)}{X_2(s)}\right|_{x_1=0} = \dfrac{1}{s+a_{22}} \cdot \dfrac{1}{1+\beta A} = \dfrac{s+a_{11}}{D(s)} \end{cases} \tag{12}$$

which can be written in the following format

$$H(s) \doteq \begin{pmatrix} H_{11} & H_{12} \\ H_{21} & H_{22} \end{pmatrix} = \frac{1}{D(s)} \cdot \begin{pmatrix} s+a_{22} & a_{21} \\ -a_{12} & s+a_1 \end{pmatrix} \tag{13}$$

Therefore, the complex output becomes

$$\begin{aligned} Y_c(s) &\doteq \mathcal{L}\{y_1(t) + j y_2(t)\} = Y_1(s) + j Y_2(s) \\ &= (H_{11}(s) X_1(s) + H_{21}(s) X_2(s)) \\ &\quad + j(H_{12}(s) X_1(s) + H_{22})(s) X_2(s) \\ &= (H_{11}(s) + j H_{12}(s)) X_1(s) + (H_{22}(s) \\ &\quad - j H_{21}(s)) j X_2(s) \\ &= \frac{s + a_{22} + j a_{21}}{D(s)} X_1(s) \\ &\quad + \frac{s + a_{11} + j a_{12}}{D(s)} j X_2(s) \end{aligned} \tag{14}$$

C. Imperfect Pole-Zero Cancellation

Let us take a closer look to $H_{cm}(s)$ and $H_{df}(s)$ given by equation (4). Their poles are given by the roots of $D(s)$. Since all the coefficients of $D(s)$ are positive real numbers, it has complex conjugate roots, i.e., $D(s) = (s-p)(s-p^*) = (s-p_1)(s-p_2)$, where

$$\begin{aligned} D(s) = 0 \quad \Rightarrow \quad s = p_{1,2} &= -\frac{a_{11}+a_{22}}{2} \\ &\pm \frac{1}{2}\sqrt{(2j)^2 a_{12} a_{21} + (a_{11}-a_{22})^2} \end{aligned} \tag{15}$$

The zero z_{cm} of $H_{cm}(s)$ is given by

$$\begin{aligned} H_{cm}(s) = 0 \quad \Rightarrow \quad s &= z_{cm} \\ &= -\frac{a_{11}+a_{22}}{2} - j\frac{a_{12}+a_{21}}{2} \end{aligned} \tag{16}$$

In order to compare the location of p_2 and z_{cm}, let us assume that $a_{21} = a_{12}(1+\Delta_b)$ and $a_{22} = a_{11}(1+\Delta_a)$; equations (15) and (16) become

$$\begin{cases} p_2 = -\dfrac{a_{11}+a_{22}}{2} - j\sqrt{a_{12}a_{21} - \dfrac{1}{4}(a_{11}-a_{22})^2} \\ \quad \cong -\dfrac{a_{11}+a_{22}}{2} - j a_{12}\sqrt{1+\Delta_b + \dfrac{a_{11}}{4a_{12}}\Delta_a^2} \\ z_{cm} = -\dfrac{a_{11}+a_{22}}{2} - j\dfrac{a_{12}+a_{21}}{2} = -\dfrac{a_{11}+a_{22}}{2} \\ \quad - j a_{12}\left(1 + \dfrac{\Delta_b}{2}\right) \end{cases} \tag{17}$$

Since for small values of Δ, Δ^2 is negligible, and $1 + \frac{\Delta}{2}$ is the Maclaurin's series expansion of $\sqrt{1+\Delta}$, equation (17) shows that $z_{cm} \cong p_2$, that is, the pole-zero cancellation in $H_{cm}(s)$ still occurs at a very good approximation. In conclusion, the response of $H_{cm}(\omega)$ is expected to be a "shifted" version of $H_{id}(\omega)$. On the other hand, $H_{df}(s)$ holds the same poles as $H_{cm}(s)$, but it has no finite zeros and it has a small gain—directly proportional with the magnitude of Δ_a and Δ_b.

Acknowledgments

Useful discussions with Dr. Mihai Banu of Agere Systems are gratefully acknowledged.

Notes

1. In Figs. 6 and 9 the errors were kept larger than the practical value of 1% in order to show meaningful pole-zero constellations.
2. Note that the Fourier-transform pair of $x^*(t)$ is $X^*(-\omega)$, since $\mathcal{L}\{x^*(t)\} = X^*(s^*)$ [13, p. 691].
3. Trigonometrical reminder: $\sin(\phi + \frac{\pi}{2}) = \cos(\phi)$, $\cos(\phi - \frac{\pi}{2}) = \sin(\phi)$, $\sin(\phi - \frac{\pi}{2}) = -\cos(\phi)$, $\cos(\phi + \frac{\pi}{2}) = -\sin(\phi)$, $\sin(\phi \pm \pi) = -\sin(\phi)$, and $\cos(\phi \pm \pi) = -\cos(\phi)$.
4. The H parameters defined by equation (12) are different from the traditional h parameters [16, Appendix B] of two-port circuits.

References

1. Abidi, A. A., "Direct-conversion radio transceivers for digital communications." *IEEE Journal of Solid-State Circuits* 30(12), pp. 1399–1410, 1995.

2. Razavi, B., "Design considerations for direct-conversion receivers." *IEEE Journal of Solid-State Circuits* 44(6), pp. 428–435, 1997.
3. Gabor, D., "Theory of communication." *Journal of the Institution of Electrical Engineers* 93(Part III), pp. 429–457, 1946.
4. Gingell, M. J., "A symmetrical polyphase network." U.S. Patent 3,559,042, 1968.
5. Gingell, M. J., "The synthesis and application of polyphase networks with sequence asymmetric properties." Ph.D. Thesis, Faculty of Engineering, University of London. http://users.vnet.net/gingell/, 1975.
6. Lang, G. R. and Brackett, P. O., "Complex analogue filters," in *Proceedings of the European Conference on Circuit Theory and Design,* pp. 412–419, 1981.
7. Snelgrove, W. M. and Sedra, A. S., "State-space synthesis of complex analog filters," in *Proceedings of the European Conference on Circuit Theory and Design,* pp. 420–424, 1981.
8. Sedra, A. S., Snelgrove, W. M. and Allen, R., "Complex analog bandpass filters designed by linearly shifting real low-pass prototypes," in *Proceedings of the IEEE International Symposium on Circuits and Systems,* pp. III.1223–III.1226, 1985.
9. Crols, J. and Steyaert, M. S., "A single-chip 900 MHz CMOS receiver front-end with a high performance low-IF topology." *IEEE Journal of Solid-State Circuits* 30(12), pp. 1483–1492, 1995.
10. Jantzi, S. A., Martin, K. W. and Sedra, A. S., "Quadrature bandpass delta-sigma modulation for digital radio." *IEEE Journal of Solid-State Circuits* 32(12), pp. 1935–1950, 1997.
11. Prodanov, V., Palaskas, G., Glas, J. and Boccuzzi, V., "A CMOS AGC-less IF strip for Bluetooth," in *IEEE European Solid-State Circuits Conference, Digest of Technical Papers,* pp. 488–491, 2001.
12. Jantzi, S. A., "Quadrature bandpass delta-sigma modulation for digital radio." Ph.D. Thesis, Electrical and Computer Engineering, University of Toronto, 1997.
13. Oppenheim, A., Willsky, A. S. and Nawab, S. H., *Signals and Systems*. Prentice-Hall, New Jersey, 1996.
14. Oppenheim, A. and Schafer, R. W., *Discrete-Time Signal Processing*. Prentice-Hall, New Jersey, 1998.
15. Papoulis, A., *Signal Analysis*. McGraw-Hill, New York, 1977.
16. Sedra, A. S. and Smith, K. C., *Microelectronic Circuits*. Oxford University Press: New York, 1998.

Péter Kiss received the Engineer's, M.S. and Ph.D. degrees, all in electrical engineering, from the Technical University of Timişoara, Romania, in 1994, 1995 and 2000, respectively. From 1998 to 2000 he was a research scholar at Oregon State University, Corvallis, OR, working on correction techniques for fast and accurate and large-bandwidth delta-sigma converters. Since 2001 he has been with Agere Systems (formerly part of Bell Laboratories) in Murray Hill, NJ, dealing with data converters and analog filters for wireless application. His past work involved adaptive fuzzy systems and image processing.

Vladimir Prodanov is an analog circuit designer with Communication Circuits Dept., Agere Systems (formerly Silicon Circuits Research Dept., Bell Laboratories, Lucent Technologies). Mr. Prodanov is also an adjunct professor at Columbia University, New York City, where he teaches analog and RF circuit design. Mr. Prodanov received B.S. degree from Technical University, Sofia, Bulgaria, and M.S. and Ph.D. from State University of New York at Stony Brook, in 1991, 1995 and 1997, respectively.

Jack Glas received M.Sc. (with honors) and Ph.D. degrees in electrical engineering from Delft

University of Technology in the Netherlands in 1992 and 1996, respectively. After graduation he joined Bell Laboratories (Lucent Technologies) where he continued research in the areas of RF System Design and Baseband Signal Processing algorithms. His focus has been on advanced architectures that reduce cost and power consumption while maintaining performance. Some of the systems he has been working on include Cellular systems (such as GSM) as well as Wireless LAN systems (such as 802.11a/b/g, Bluetooth). Currently he is part of the Wireless Circuits Research Department of Agere Systems where he is looking into next generation Wireless LAN systems.